Science Advances
AAAS

Supplementary Materials for

High–spatiotemporal resolution deuterium metabolic imaging enables in vivo phenotyping of intra- and intertumoral heterogeneity

Xinjie Liu *et al.*

Corresponding author: Lucio Frydman, lucio.frydman@weizmann.ac.il; Qingjia Bao, qingjia.bao@apm.ac.cn

Sci. Adv. **12**, eaef4377 (2026)
DOI: 10.1126/sciadv.aef4377

This PDF file includes:

Section 1 Iterative Reconstruction Algorithm for MF-bSSFP

The MF-bSSFP signals S_n arising from multiple metabolites (main text, Equation (2)) contain M+1 complex unknowns: $\{\rho_m\}_{\mathrm{m=1,2,\ldots,M}}$, and f_b. In general, M+1 or more images with different frequency offsets f_n are required to determine the system and separate all chemical species. For example, in a system with water, glucose and lactate, at least four images are thus required; however, to ensure robustness in the reconstruction, usually one more signal is to be acquired. The field map required for the ensuing non-Fourier reconstruction was acquired through multi-echo GRE. The initial estimate of f_{b0} is known, so Equation (2) (main text) can be rewritten as

$$S_n' = S_n e^{-i2\pi f_{b0} TE} = \sum_{m=1}^{M} \rho_m M S_m e^{i2\pi (f_m + f_n) TE} \tag{S1}$$

Equation (S1) forms a set of linear equations that are amenable to linear least-squares fitting to decompose initial estimates of each chemical species ρ_m'.

In the actual reconstruction used, the initial estimate of the field map f_{b0} was refined further by defining error terms: $f_b = f_{b0} + \Delta f_b$, $\rho_m = \rho_m' + \Delta\rho_m$. Inserting these expressions into Equation (2) (main text), it can be rewritten as:

$$S_n = e^{i2\pi (f_{b0} + \Delta f_b) TE} \sum_{m=1}^{M} (\rho_m' + \Delta\rho_m) M S_m e^{i2\pi (f_m + f_n) TE} \tag{S2}$$

Dividing each side by $e^{i2\pi f_{b0} TE}$, and using the Taylor approximation $e^{-i2\pi \Delta f_{b0} TE} \approx 1 + i2\pi\Delta f_{b0} TE$:

$$S_n'' \approx S_n' + \sum_{m=1}^{M} \Delta\rho_m M S_m e^{i2\pi (f_m + f_n) TE} + i2\pi\Delta f_{b0} TE \sum_{m=1}^{M} \rho_m' M S_m e^{i2\pi (f_m + f_n) TE} + i2\pi\Delta f_{b0} TE \sum_{m=1}^{M} \Delta\rho_m M S_m e^{i2\pi (f_m + f_n) TE} \tag{S3}$$

Since Δf_{b0} and $\Delta\rho_m$ are two small quantities multiplied, the last term of the Equation (S3) can be omitted and the result written as:

$$S_n'' \approx S_n' + \sum_{m=1}^{M} \Delta\rho_m M S_m e^{i2\pi (f_m + f_n) TE} + i2\pi\Delta f_{b0} TE \sum_{m=1}^{M} \rho_m' M S_m e^{i2\pi (f_m + f_n) TE} \tag{S4}$$

The estimates of Δf_{b0} and $\Delta\rho_m$ can thus be calculated in a least-squares sense.

Using the above equations, the following algorithm summarizes the method used to determine the least-squares estimates of metabolite images for each pixel:

i. Estimate the signal from each chemical species using Equation (S4) (main text) and an initial guess for the field map, A useful initial guess for f_{b0} is acquired by multi-echo GRE.

ii. Calculate the error to the field map, Δf_{b0}, using Equation (S4).
iii. Recalculate $f_b = f_{b0} + \Delta f_b$.
iv. Recalculate S_n with the new estimate of f_b.
v. Repeat the preceding three steps until Δf_{b0} is small.
vi. Spatially filter (smooth) the final field map f_b with a low-pass filter.
vii. Recalculate the final estimate of each chemical species image with Equation (S4).

Then, the concentration of substrates and metabolites was calculated by comparing the ^{2}H NMR signals to ^{2}H/HOD signal (10.12 mM):

$$CON_m = \frac{\rho_m}{\rho_{water} \cdot ND} \cdot CON_{water} \quad \text{(S5)}$$

where CON_m refers to the concentrations of substrates and metabolites, ρ_m and ρ_{water} represents the MR signal of metabolites and water, ND represents the average number of deuterons per molecule, and CON_{water} refers to the ^{2}H/HOD concentration.

Section 2 Figures

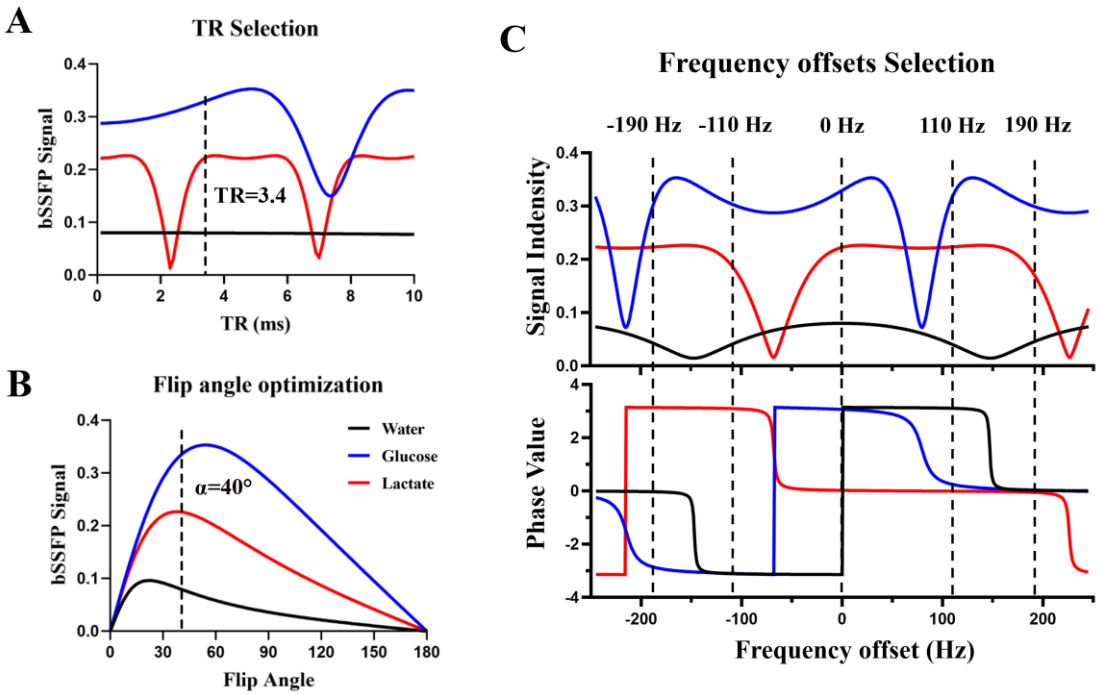

Figure S1. MF-bSSFP sequence optimization. (A) Signal intensity curves of three metabolites (water in black; glucose in blue; lactate in red) as a function of TR in bSSFP simulation, with optimal TR determined at 3.4 ms. **(B)** Simulated signal intensities of three metabolites as a function of flip angle in bSSFP (9.4T), with optimal flip angle at 40°. **(C)** Simulated bSSFP signal intensity and phase curves of three metabolites at different frequency offsets according to the formulas and simulation parameters (water, 4.8 ppm; glucose, 3.7 ppm; lactate, 1.3 ppm; TR, 3.4 ms; flip angle, 40°), with optimal frequency offsets determined at -190 Hz, -110 Hz, 0 Hz, 110 Hz, 190 Hz.

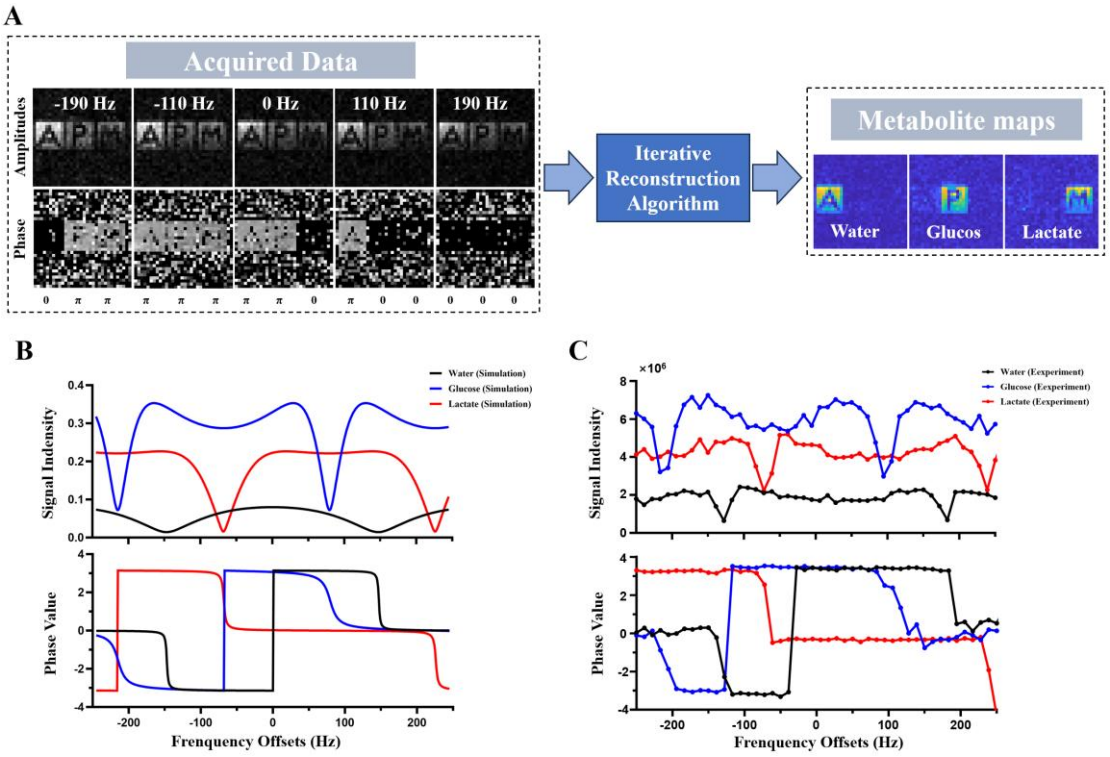

Figure S2. Phantom validation of the reconstruction algorithm and bSSFP signal model. (A) ^{2}H magnitude and phase images acquired with MF-bSSFP at five frequency offsets (–190, –110, 0, +110, +190 Hz). Magnitude images showed comparable signal intensities across metabolites, whereas phase images exhibited distinct frequency-dependent contrasts consistent with simulations. These phase signatures were used by the iterative reconstruction algorithm to separate spatial metabolite distributions. **(B)** Simulated bSSFP signal intensity (top) and phase (bottom) responses of $^{2}H_2O$, [6,6'-$^{2}H_2$]-glucose, and [3,3,3-$^{2}H_3$]-lactate under optimized parameters. The simulated curves are the same source plots as those in Fig. S1C and are reused here to facilitate direct comparison with the phantom measurements in panel C. **(C)** Experimental bSSFP signal intensities (top) and phases (bottom) measured in a phantom containing $^{2}H_2O$ (40 mM), [6,6'-$^{2}H_2$]-glucose (20 mM), and [3,3,3-$^{2}H_3$]-lactate (20 mM). Signal intensities were adjusted according to metabolite concentrations. Overall, the experimental data closely matched the simulations, confirming the accuracy of the signal model.

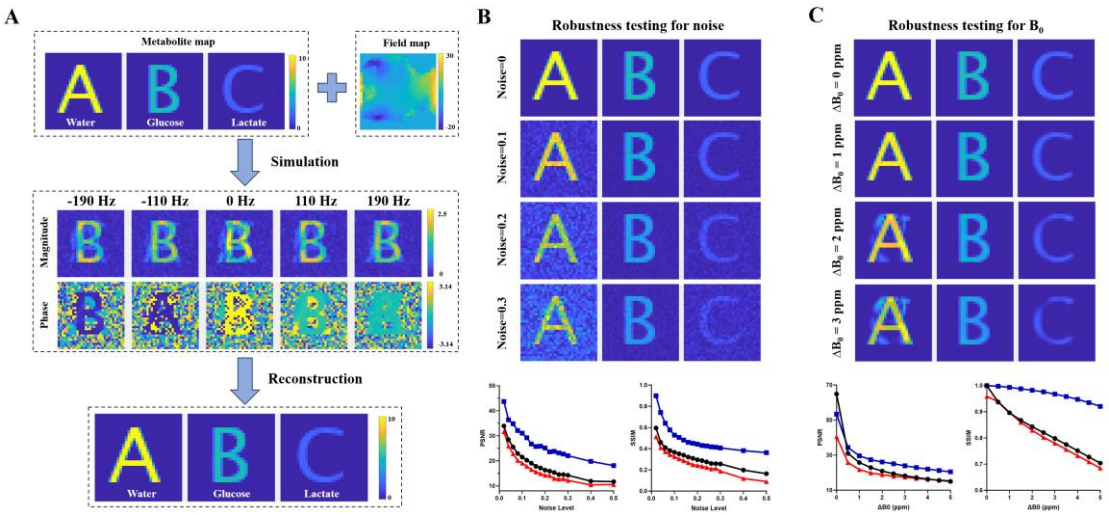

Figure S3. MF-bSSFP simulation and robustness analysis against noise and B_0 inhomogeneity. (A) Simulation and reconstruction workflow. Row 1: simulated metabolite maps (A = water, B = glucose, C = lactate) combined with a field map from real experiments. Row 2: simulated magnitude and phase images at five frequency offsets (–190, –110, 0, +110, +190 Hz). Row 3: reconstructed metabolite maps after separation. **(B)** Robustness to noise. Rows 1–4: reconstructed metabolite maps at noise levels of 0, 0.1, 0.2, and 0.3. Row 5: Peak Signal-to-Noise Ratio (PSNR) and Structural Similarity Index (SSIM) as a function of noise level for water (black), glucose (blue), and lactate (red). Noise varied from 0 to 0.5, with 0.02 increments for 0–0.3 and 0.1 increments for 0.3–0.5. **(C)** Robustness to B_0 inhomogeneity. Rows 1–4: reconstructed metabolite maps at B_0 offsets of 0, 1, 2, and 3 ppm. Row 5: PSNR and SSIM as a function of B_0 inhomogeneity for water (black), glucose (blue), and lactate (red), sampled from 0 to 5 ppm in 0.5 ppm steps.

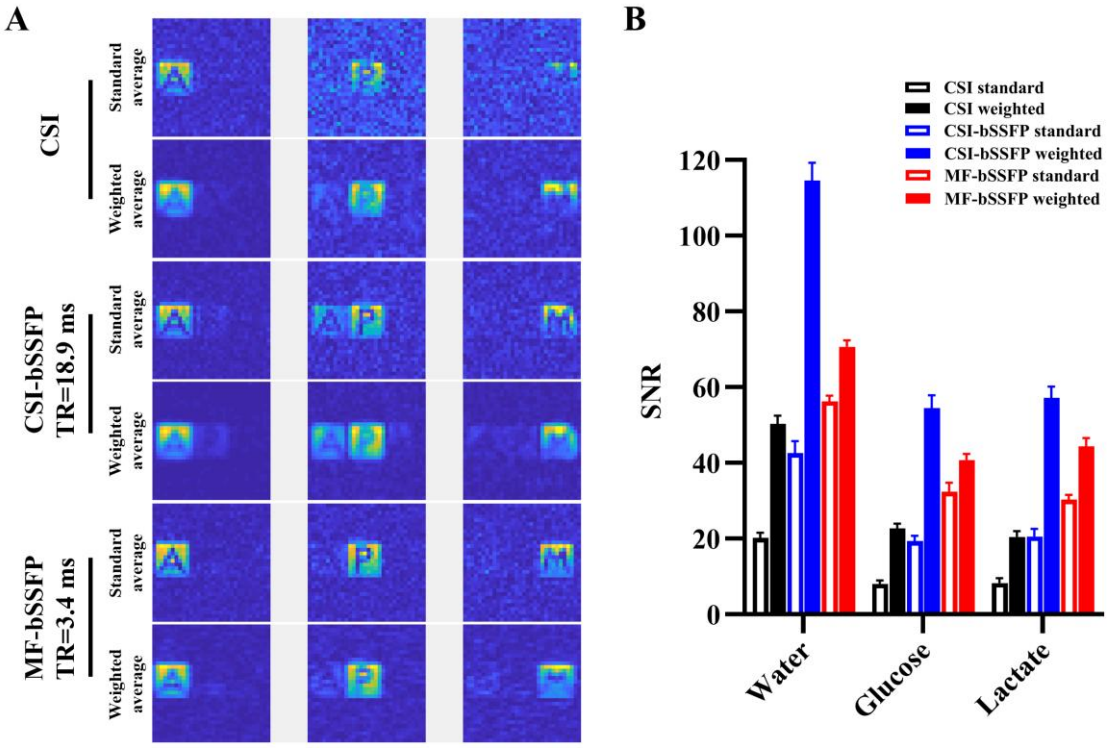

Figure S4. Phantom experiment results and comparison among CSI, CSI-bSSFP, and MF-bSSFP with standard average and weighted average. (A) The phantom study consisted of $^{2}H_2O$ ('A', ~40 mM), [6,6'-$^{2}H_2$]-glucose ('P', ~20 mM), and [3,3,3-$^{2}H_3$]-lactate ('M', ~20 mM) in separate tubes. Around 5 min scan times; 32×32 matrices; 30×30 mm^2 FOVs. Water, glucose, and lactate images obtained from the three methods. Left row 1: CSI with standard average; Left row 2: CSI with 2D weighted average; Left row 3: CSI-bSSFP with standard average; Left row 4: CSI-bSSFP with 2D weighted average; Left row 5: MF-bSSFP with standard average; Left row 6: MF-bSSFP with 1D weighted average. Some metabolite maps shown in panel A are the same source images as those shown in Fig. 2 and are reused here to facilitate direct comparison of the different acquisition and averaging strategies. **(B)** SNR comparison for water, glucose and lactate from the left (Water: CSI standard, 20.18±1.40, CSI weighted, 50.21±2.28, CSI-bSSFP standard, 42.58±3.15, CSI-bSSFP weighted, 114.58±4.66, MF-bSSFP standard, 56.29±1.44, MF-bSSFP weighted, 70.68±1.67; Glucose: CSI standard, 8.00±0.91, CSI weighted, 22.63±1.30, CSI-bSSFP standard, 19.36±1.38, CSI-bSSFP weighted, 54.41±3.41, MF-bSSFP standard, 32.40±2.32, MF-bSSFP weighted, 40.74±1.63; Lactate: CSI standard, 8.24±1.40, CSI weighted, 20.42±1.49, CSI-bSSFP standard, 20.55±1.98, CSI-bSSFP weighted, 57.20±2.97, MF-bSSFP standard, 30.23±1.32, MF-bSSFP weighted, 44.39±2.13). All the methods with weighted average improved the images' SNR compared to that with standard average. Both CSI-bSSFP and MF-bSSFP improved the images' SNR compared to CSI.

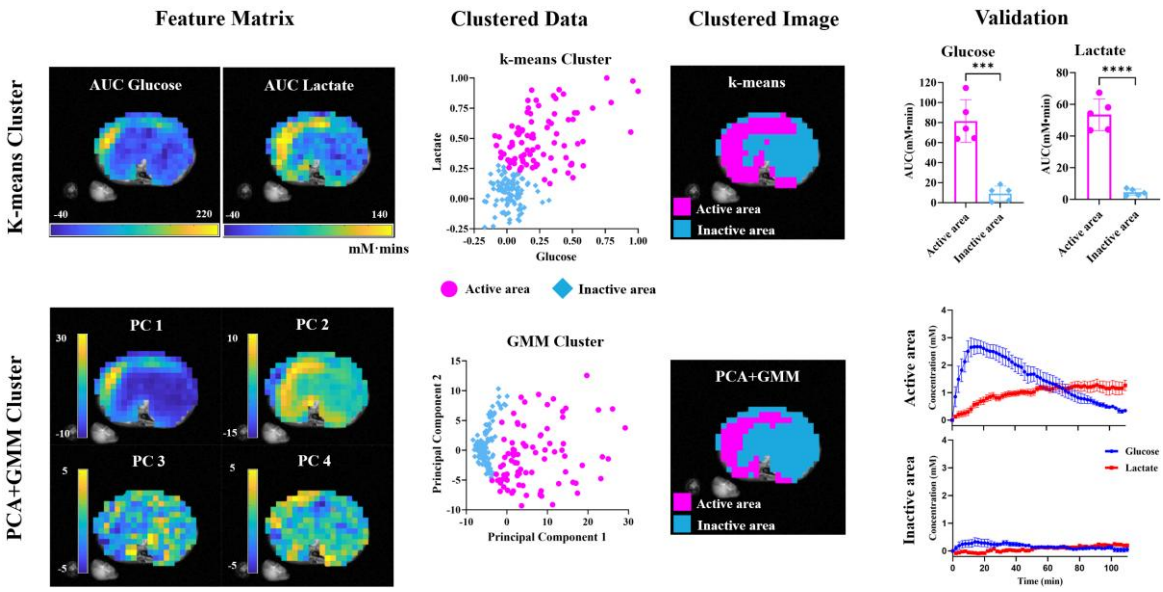

Figure S5. Unsupervised clustering of high-resolution DMI delineates viable vs necrotic tumor subregions. Top row (k-means pipeline): Feature matrix composed of glucose and lactate AUC maps (left); voxel-wise scatter of normalized AUC values and k-means labels (middle); clustered DMI map showing active (magenta) and inactive (blue/cyan) areas (right); bar plots (top right) showing significantly higher glucose and lactate AUC in active vs inactive regions (***p < 0.001, ****p < 0.0001; bars = mean ± SD). **Bottom row (PCA+GMM pipeline):** Feature matrix of the first four principal components (PC1–PC4) derived from the concatenated dynamic glucose and lactate time courses (left); voxels projected onto the first two PCs and clustered by GMM (middle); corresponding clustered DMI map (right). Dynamic concentration curves further confirm that active metabolic regions exhibited high glucose enrichment and lactate accumulation, whereas inactive regions show minimal glucose enrichment and negligible lactate accumulation. The images and plots shown in the top row are the same source data as those shown in Figs. 1B and 3A and are reused here for direct comparison with the PCA+GMM results in the bottom row.

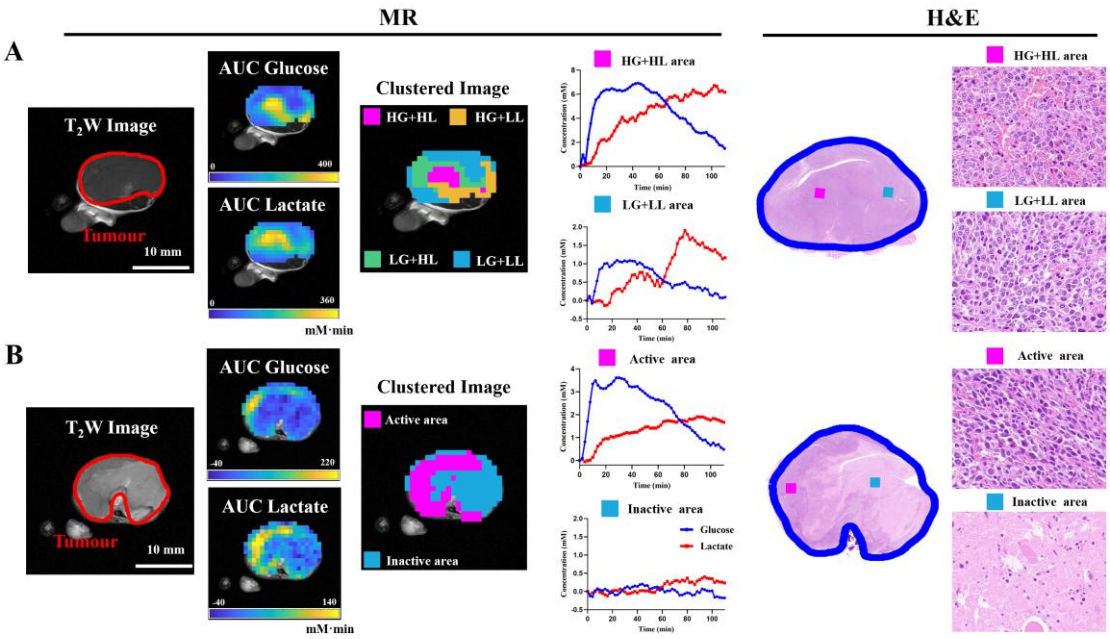

Figure S6. Comparing intratumoral metabolic heterogeneity with and without necrosis. (A) K-means clustering of tumors without necrosis tissue identifies four metabolic phenotypes—*HG+HL*, *HG+LL*, *LG+HL*, and *LG+LL*. Cluster-specific time courses reveal distinct metabolic activities across all subgroups. Histology confirms the absence of macroscopic necrosis, including within *LG+LL* (low-metabolic) areas. The regional histology images labeled HG+HL area and LG+LL area are magnified views of the magenta- and cyan-boxed regions, respectively, in the corresponding whole-section H&E image. The MR and clustering images are the same source images as those shown in Fig. 4 and histology images are the same source images as those shown in Fig. 5. And they are reused here for comparison between tumors with and without necrosis. **(B)** K-means clustering separates the tumor with necrosis into active and inactive compartments. Dynamic curves show robust glucose enrichment and lactate accumulation in active tissue, whereas inactive regions display near-flat signals, clearly distinct from *LG+LL* areas (low but non-zero metabolism). H&E staining validates extensive necrosis within the necrotic compartment. The regional histology images labeled HG+HL area and LG+LL area are magnified views of the magenta- and cyan-boxed regions, respectively, in the corresponding whole-section H&E image. Some images are the same source images as those shown in Figs. 1 and 3 and are reused here to facilitate direct comparison between tumors with and without necrosis. DMI-based clustering reliably distinguishes hypometabolic yet viable tissue (e.g., *LG+LL*) from frank necrosis by leveraging both amplitude and temporal features of ^{2}H-glucose/^{2}H-lactate signals. In viable but hypometabolic voxels, glucose and lactate AUCs are low but non-zero and their time courses exhibit measurable uptake/production kinetics; in contrast, necrotic voxels show near-zero AUCs with flat dynamics approaching baseline noise. Histological staining validated the presence of extensive necrosis within the necrotic area.

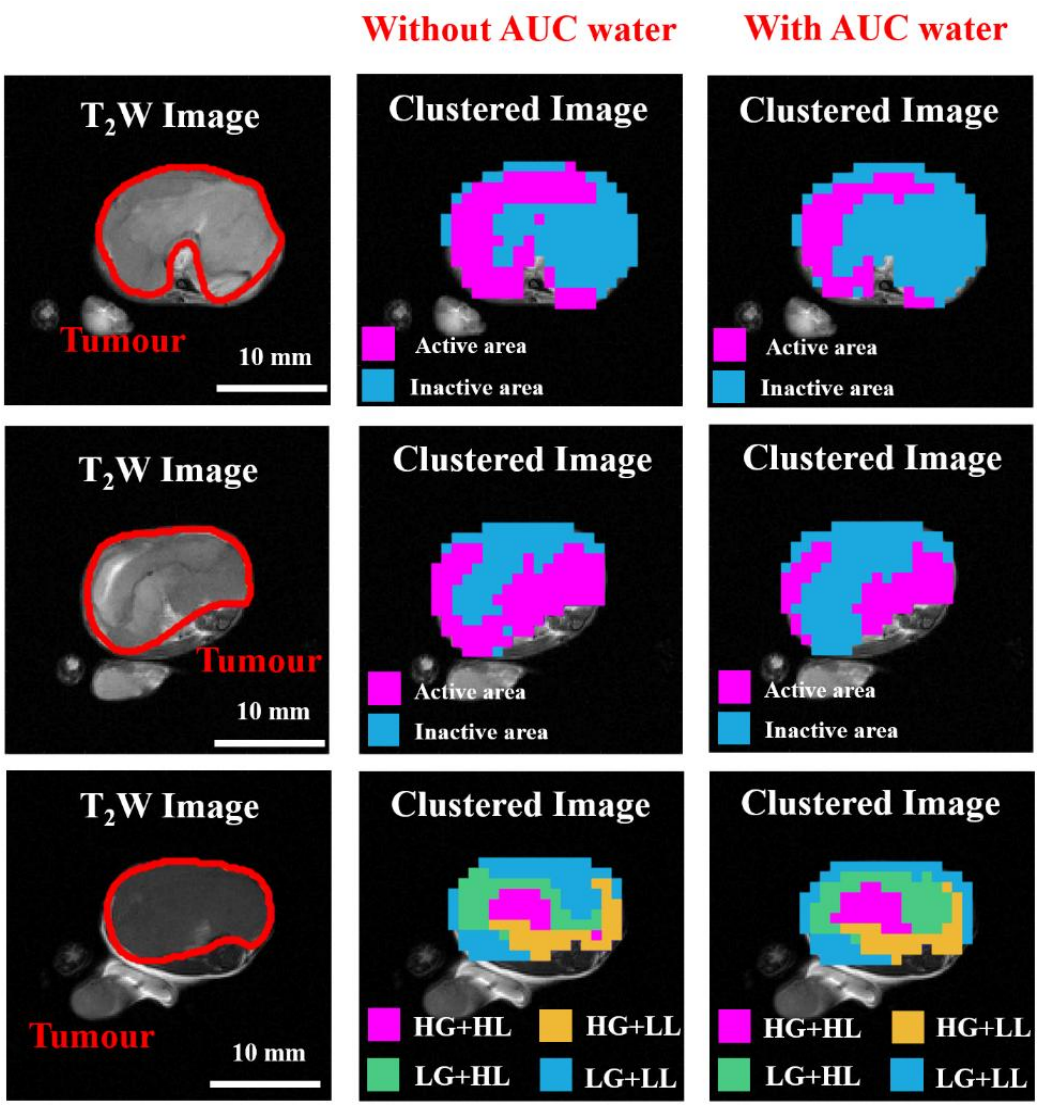

Figure S7. Comparison of clustering results with and without inclusion of AUC water in the analysis. Left column: T_2-weighted anatomical images with tumor regions outlined in red. Middle column: voxel-wise clustering results based on glucose and lactate metrics (without AUC water). Right column: clustering results after inclusion of AUC water. These findings indicate that inclusion of AUC water does not substantially alter voxel-wise metabolic classification. The T_2-weighted images and clustered images in the middle columns are the same source images as those shown in Figs. 1, 3, and 4 and are reused here to facilitate direct comparison with the clustering results obtained after inclusion of AUC water.

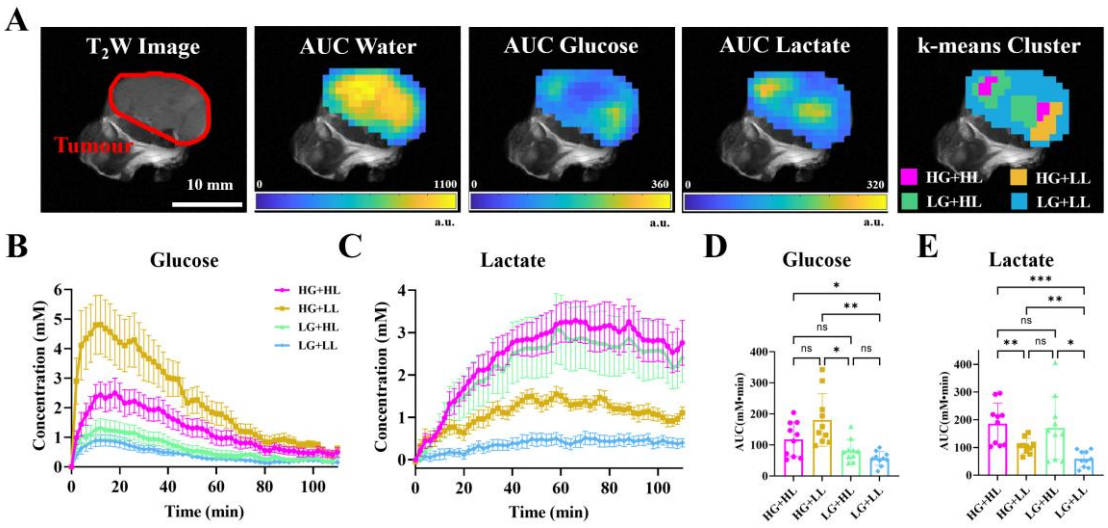

Figure S8. k-mean clustering and quantitative analysis on ten CT26 tumor-bearing mice. (A) Axial ^{1}H T_2-weighted anatomical image and AUC maps of ^{2}H-water, ^{2}H-glucose, and ^{2}H-lactate. The distribution of water was relatively uniform, whereas glucose and lactate exhibited marked spatial heterogeneity. And spatial map of the four identified metabolic phenotypes: *HG+HL*, *HG+LL*, *LG+HL*, and *LG+LL*. The images are the same source images as those in Fig. 6 and are reused here to facilitate direct comparison with the summary analyses in panels B to E. **(B, C)** Time-resolved metabolic curves of glucose **(B)** and lactate **(C)** concentrations for each cluster on all 10 CT26 tumor-bearing mice. **(D)** Quantification of glucose AUC values across clusters of 10 CT26 tumor-bearing mice. Glucose enrichment was significantly higher in HG+HL and HG+LL areas compared to *LG+HL* and *LG+LL* (*HG+HL*: 118.3 ± 17.52; *HG+LL*: 180.4 ± 26.78; *LG+HL*: 81.56 ± 11.25; *LG+LL*: 56.44 ± 7.01; ns: not significant, *p < 0.05, **p < 0.01). **(E)** Quantification of lactate AUC values across clusters of all 10 CT26 tumor-bearing mice. Lactate accumulation was significantly elevated in *HG+HL* and *LG+HL* areas compared to *HG+LL* and *LG+LL* (*HG+HL*: 185.9 ± 23.56; *HG+LL*: 105.3 ± 8.58; *LG+HL*: 170.7 ± 35.60; *LG+LL*: 59.01 ± 9.17; ns: not significant, *p < 0.05, **p < 0.01, ***p < 0.001).

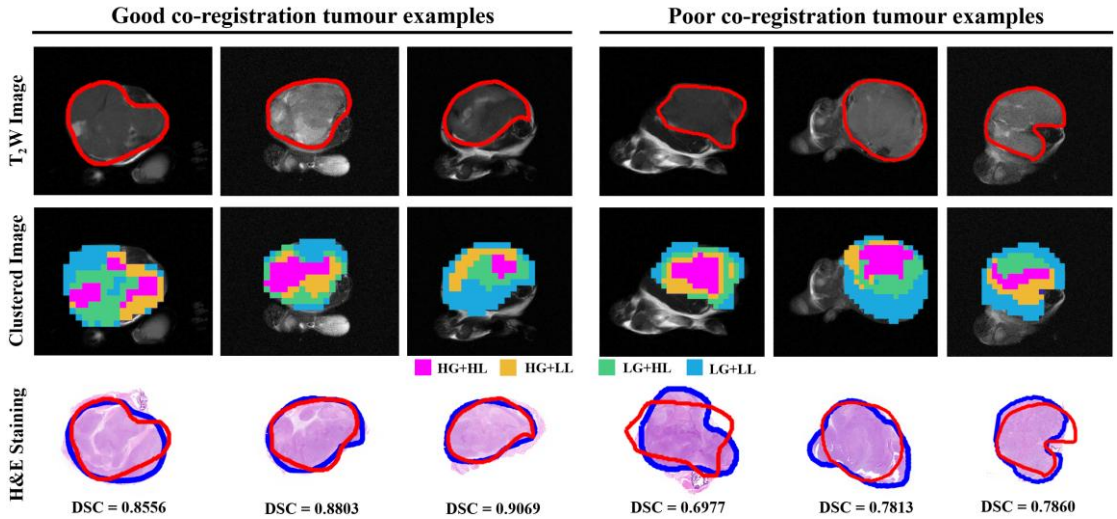

Figure S9. Tumor examples showing good and poor MRI/histology co-registration. Top to bottom: T_2W image (anatomy); clustered image with four metabolic subregions; co-registered H&E showing staining and the corresponding overlapping contours. The left three columns depict good co-registration examples (DSC= 0.8556, 0.8803, 0.9069, respectively); the right three columns depict poor co-registration examples (DSC= 0.6977, 0.7813, 0.7860, respectively).

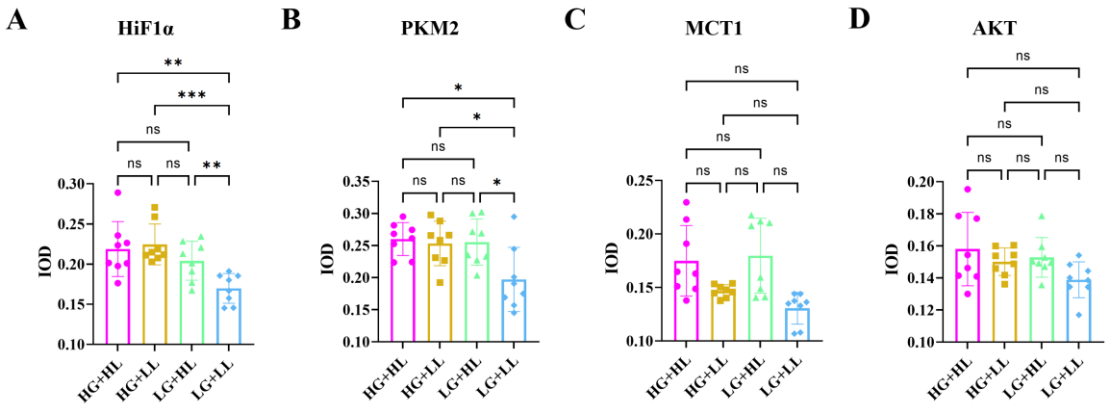

Figure S10. Statistical analysis for four metabolism-related markers that did not show good correlation with DMI-detected metabolic areas. All 8 tumor-bearing mice in this summary presented good MRI/histology spatial alignment. Integrated optical density (IOD) values of HiF1a **(A)** and PKM2 **(B)** in *HG+HL*, *HG+LL* and *LG+HL* areas are higher than *LG+LL* areas. (HiF1α: *HG+HL*, 0.2188 ± 0.0121; *HG+LL*, 0.2245 ± 0.0090; *LG+HL*, 0.2041 ± 0.0086; *LG+LL*, 0.1697 ± 0.0065; PKM2: *HG+HL*, 0.2601 ± 0.0091; *HG+LL*, 0.2533±0.0123; *LG+HL*, 0.2553 ± 0.0127; *LG+LL*, 0.1972 ± 0.0177. ns, not significant; *p < 0.05, **p < 0.01, ***p < 0.001). IOD values of MCT1 **(C)** and AKT **(D)** did not show differences among *HG+HL*, *HG+LL*, *LG+HL* and *LG+LL* areas.

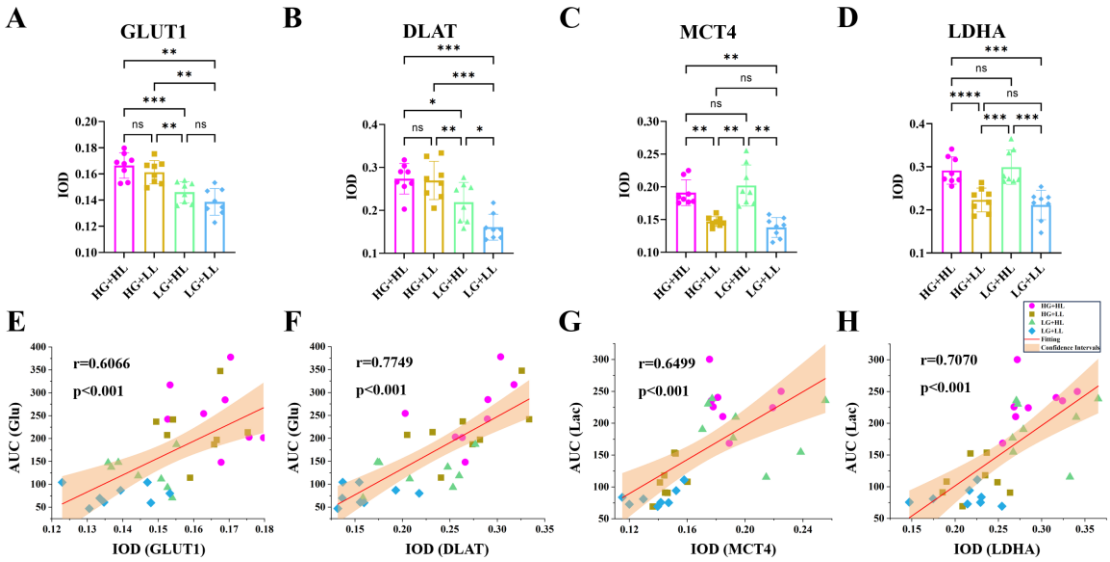

Figure S11. Statistical analysis of IHC results for eight tumor-bearing mice presenting good MRI/histology co-registration, as well as meaningful correlations between metabolism-related markers' activities (IOD) and DMI (AUC). (A–D) Quantification of metabolism-related markers expression based on IOD. GLUT1 **(A)** and DLAT **(B)** levels were significantly higher in HG areas (GLUT1: *HG+HL*, 0.1664±0.0034; *HG+LL*, 0.1613±0.0031; *LG+HL*, 0.1460±0.0029; *LG+LL*, 0.1387±0.0036. DLAT: *HG+HL*, 0.2736±0.0126; *HG+LL*, 0.2696±0.0158; *LG+HL*, 0.2192±0.0162; *LG+LL*, 0.1608±0.0106; ns, not significant; *p < 0.05, **p < 0.01, ***p < 0.001), whereas MCT4 **(C)** and LDHA **(D)** were enriched in HL areas (MCT4: *HG+HL*, 0.1911 ± 0.0069; *HG+LL*, 0.1470 ± 0.0026; *LG+HL*, 0.2020 ± 0.0111; *LG+LL*, 0.1380 ± 0.0054; LDHA: *HG+HL*, 0.2915 ± 0.0112; *HG+LL*, 0.2233±0.0098; *LG+HL*, 0.2993 ± 0.0141; *LG+LL*, 0.2115 ± 0.0121. ns, not significant; **p < 0.01, ***p < 0.001, ****p < 0.0001). **(E–H)** Voxel-wise correlation between metabolite (AUC) and metabolism-related markers expression (IOD). Glucose AUC showed positive correlations with GLUT1 (**E**, r = 0.6066, p < 0.001) and DLAT (**F**, r = 0.7749, p < 0.001). Lactate AUC was correlated with MCT4 (**G**, r = 0.6499, p < 0.001) and LDHA (**H**, r = 0.7070, p < 0.001). Shaded regions indicate 95% confidence intervals.

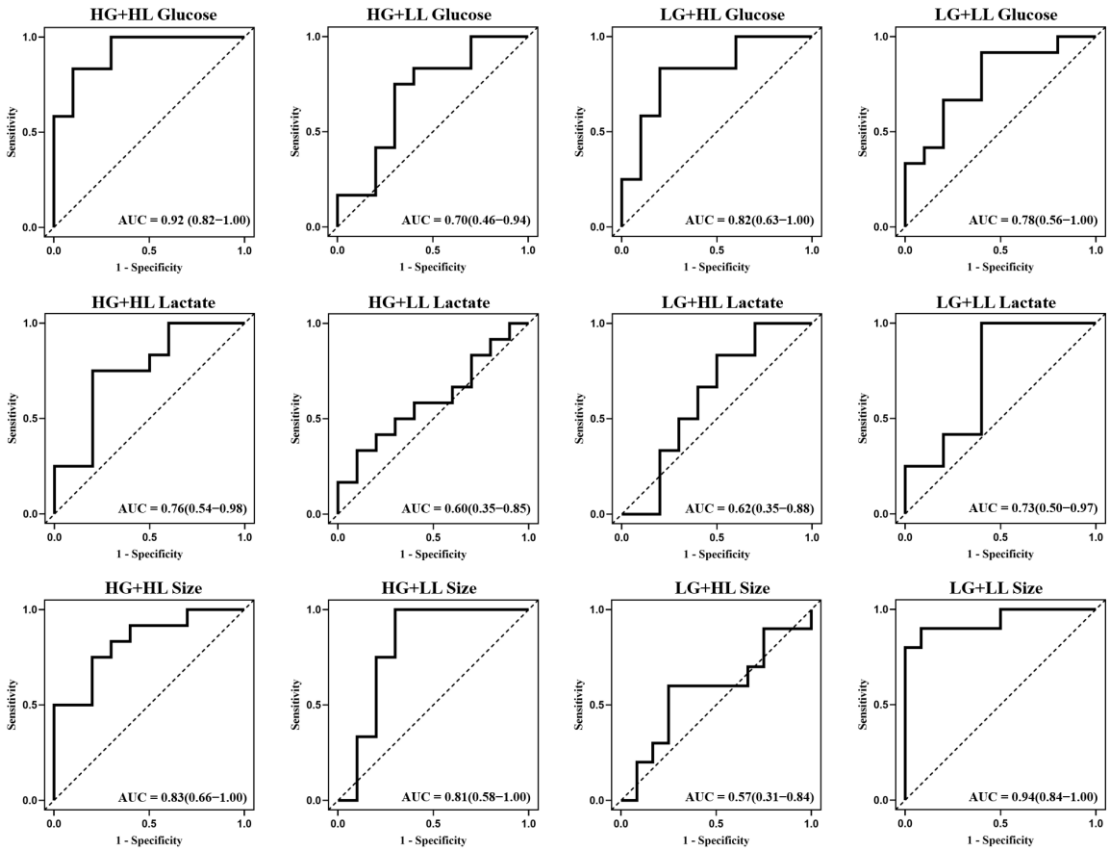

Figure S12. ROC curve analysis for features related to glucose enrichment, lactate accumulation and region size, assessing the discriminative power of metabolic features for tumor subtype classification. Among these, features with highest predictive accuracy (>0.80) are glucose concentration in the HG+HL (AUC = 0.92) and LG+HL areas (AUC = 0.82), the fractional volume of the HG+HL (AUC = 0.83), HG+LL (AUC = 0.81), and LG+LL areas (AUC = 0.94). Features with poorer predictive accuracy (<0.80) are glucose concentration in the HG+LL (AUC = 0.70) and LG+LL area (AUC = 0.78), lactate concentration in 4 areas (HG+HL: AUC = 0.76; HG+LL: AUC = 0.60; LG+HL: AUC = 0.62; LG+LL: AUC = 0.73), and the fractional volume of the LG+HL area (AUC = 0.57). Some ROC curves are the same source plots as those in Fig. 6 and are reused here to facilitate direct comparison among the different metabolic features.

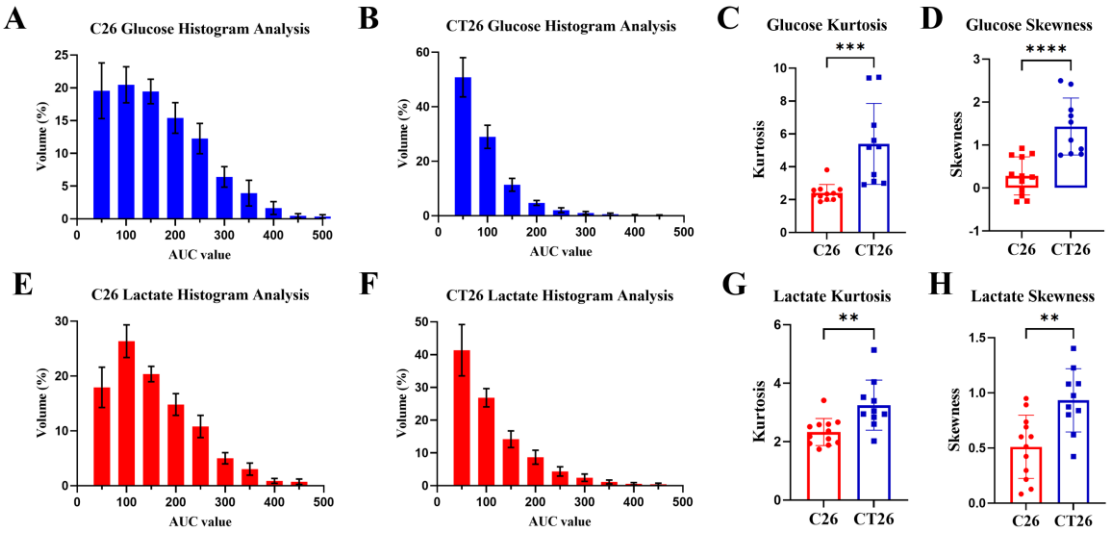

Figure S13. DMI-based frequency distribution histograms based on AUC data, revealing intertumoral metabolic heterogeneity. (A-D) Frequency distribution histogram analysis of glucose AUC values in C26 and CT26 tumor-bearing mice. Glucose AUC histograms maps of C26 **(A)** and CT26 **(B)** showing significantly different distributions. Statistical analysis of the kurtosis values **(C)** and skewness values **(D)** show higher CT26 than C26 values (Kurtosis: C26, 2.417±0.1447, CT26, 5.392±0.7781; Skewness: C26, 0.2809±0.1281, CT26, 1.432±0.2099). **(E-H)** Frequency distribution histogram analysis of lactate AUC values in C26 and CT26 tumor-bearing mice. Lactate AUC histograms maps of C26 **(E)** and CT26 **(F)** showed significantly different distributions. Statistical analysis of the kurtosis values **(G)** and skewness values **(H)** showed that the values of CT26 were higher than that of C26 (Kurtosis: C26, 2.329±0.1338, CT26, 3.250±0.2712; Skewness: C26, 0.5112±0.0829, CT26, 0.9327±0.0908).

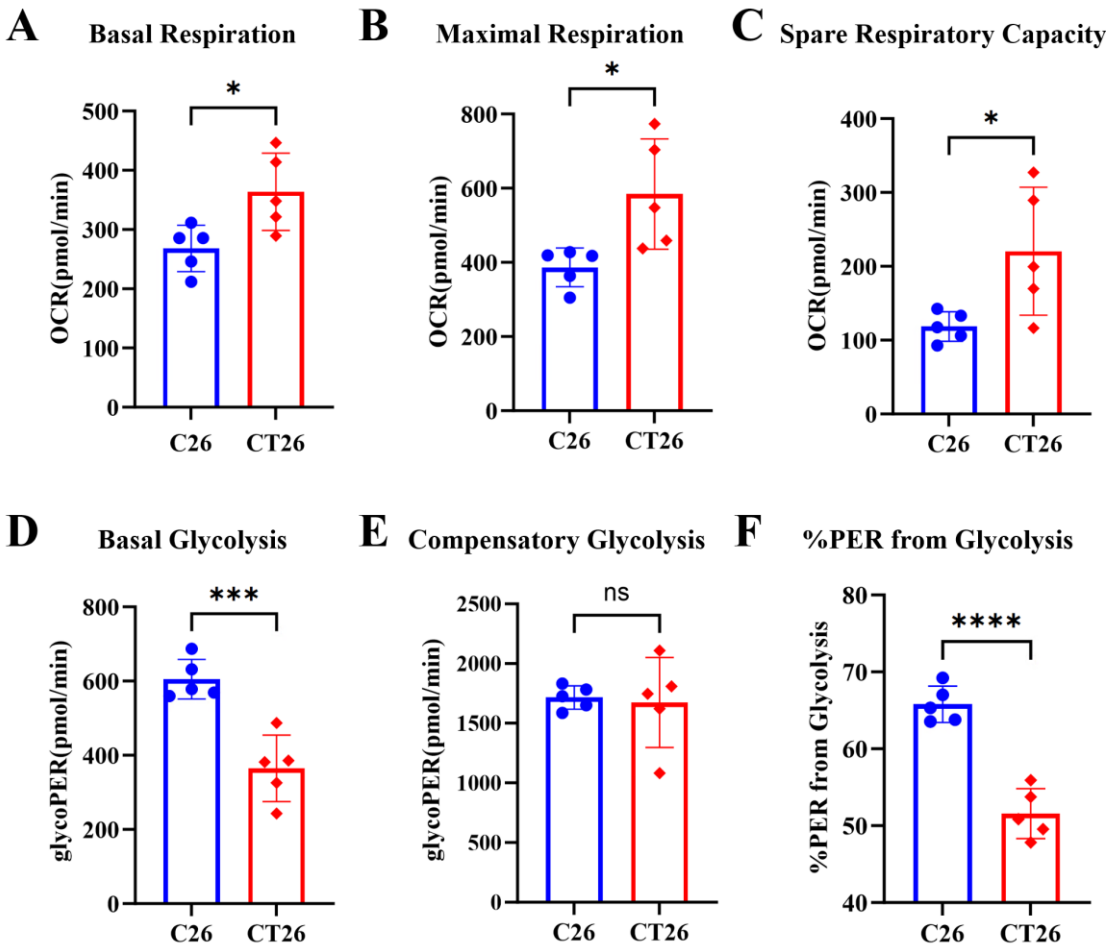

Figure S14. Seahorse-based in vitro metabolic characterization of C26 and CT26 tumor cells. (A-C) Seahorse XF Cell Mito Stress Tests including the basal respiration (**A**, C26, 268.1 ± 17.52; CT26, 363.8± 29.11. *$p < 0.05$), maximal respiration (**B**, C26, 386.5 ± 23.37; CT26, 584.3 ± 66.52. *$p < 0.05$), spare respiratory capacity (**C**, C26, 118.4 ± 8.93; CT26, 220.5 ± 38.71. *$p < 0.05$). The result indicates that mitochondrial respiration in CT26 cells is more intense than that in C26 cells. **(D-F)** Seahorse XF Glycolytic Rate Assays including the Basal Glycolysis (**D**, C26, 605.1 ± 23.95; CT26, 364.7± 39.98. ***$p < 0.001$), Compensatory Glycolysis (**E**, C26, 1716.0 ± 44.13; CT26, 1674.0 ± 168.30. ns, not significant), percentage of PER from glycolysis (**F**, C26, 65.78 ± 1.06; CT26, 51.57 ± 1.46. ****$p < 0.0001$). The result indicates that glycolytic potential in C26 cells is higher than that in CT26 cells.

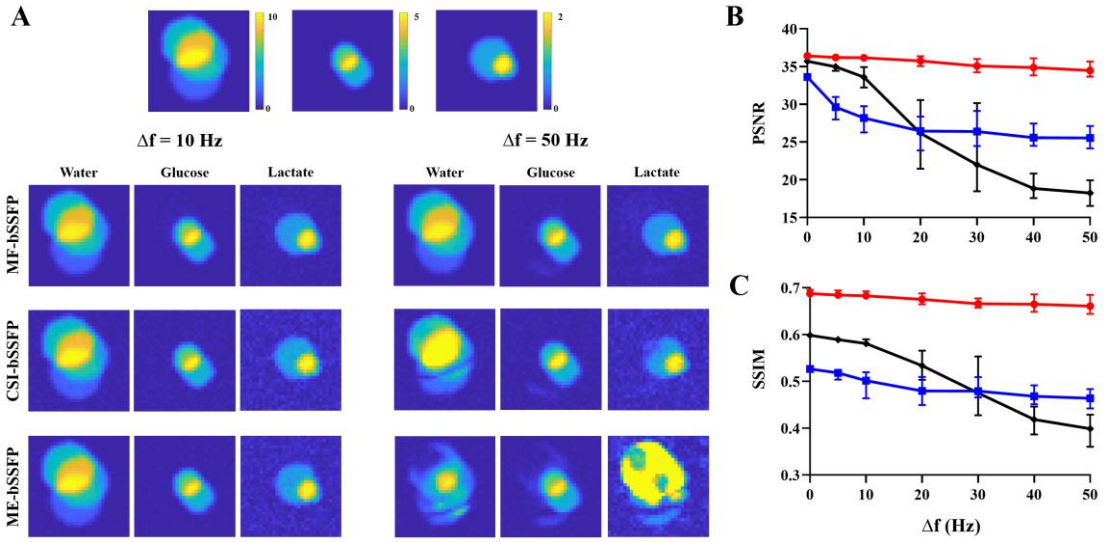

Figure S15. Simulation-based comparison of metabolite separation performance under increasing B_0 field inhomogeneity. (A) Representative reconstructed metabolite maps (water, glucose, and lactate) obtained using MF-bSSFP, CSI-bSSFP, and ME-bSSFP at frequency offsets of $\Delta f = 10$ Hz and 50 Hz. Under mild field inhomogeneity, all three methods achieve adequate metabolite separation, whereas increased B_0 offsets lead to pronounced signal mixing and incomplete compound separation in CSI-bSSFP and ME-bSSFP. In contrast, MF-bSSFP preserves robust metabolite delineation across all conditions. **(B)** Peak signal-to-noise ratio (PSNR) and **(C)** structural similarity index (SSIM) as functions of Δf, quantitatively demonstrating the superior robustness of MF-bSSFP to B_0 inhomogeneity compared with the other methods. These simulations were performed independently for B_0-robustness analysis and are not reused from Fig. S3, which illustrates the simulation workflow.

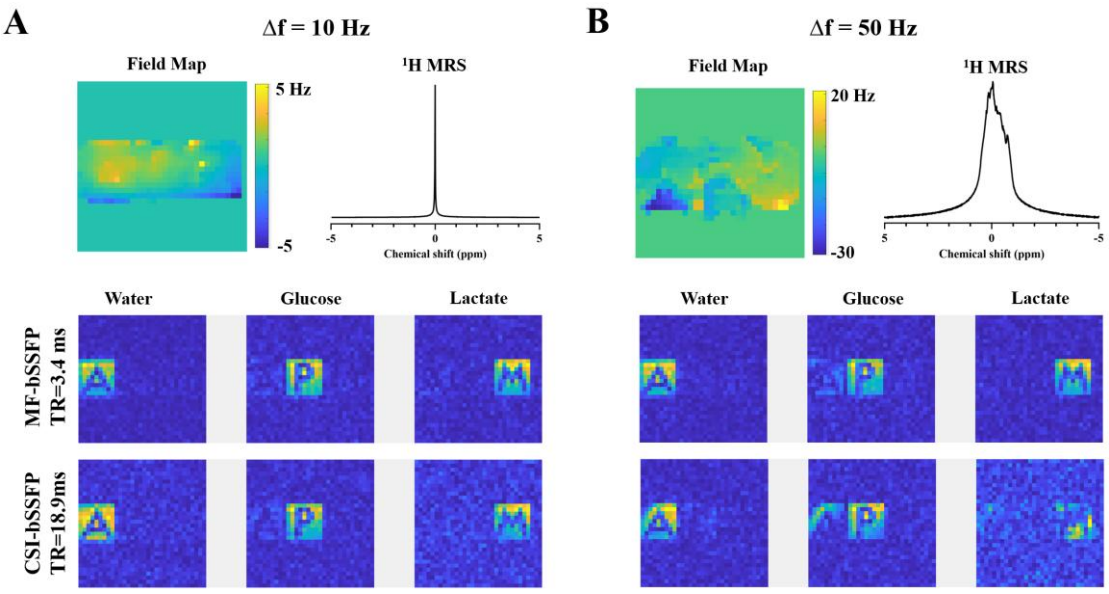

Figure S16. Phantom experiments validating metabolite separation performance under different B_0 field conditions. Representative results acquired under **(A)** relatively homogeneous B_0 conditions ($\Delta f = 10$ Hz) and **(B)** increased B_0 field inhomogeneity ($\Delta f = 50$ Hz), including the measured field map, corresponding ^{1}H MRS spectrum, and reconstructed water, glucose, and lactate maps using MF-bSSFP (TR = 3.4 ms) and CSI-bSSFP (TR = 18.9 ms). Under well-shimmed conditions, both methods achieve clear metabolite separation. Under poorly shimmed conditions, MF-bSSFP maintained robust and spatially consistent separation of individual compounds, whereas CSI-bSSFP showed degraded metabolite delineation and increased signal mixing, particularly for glucose and lactate. These data were obtained in a separate phantom experiment specifically designed to evaluate robustness to B_0 field inhomogeneity and are not reused from Fig. 2 and Fig. S4.

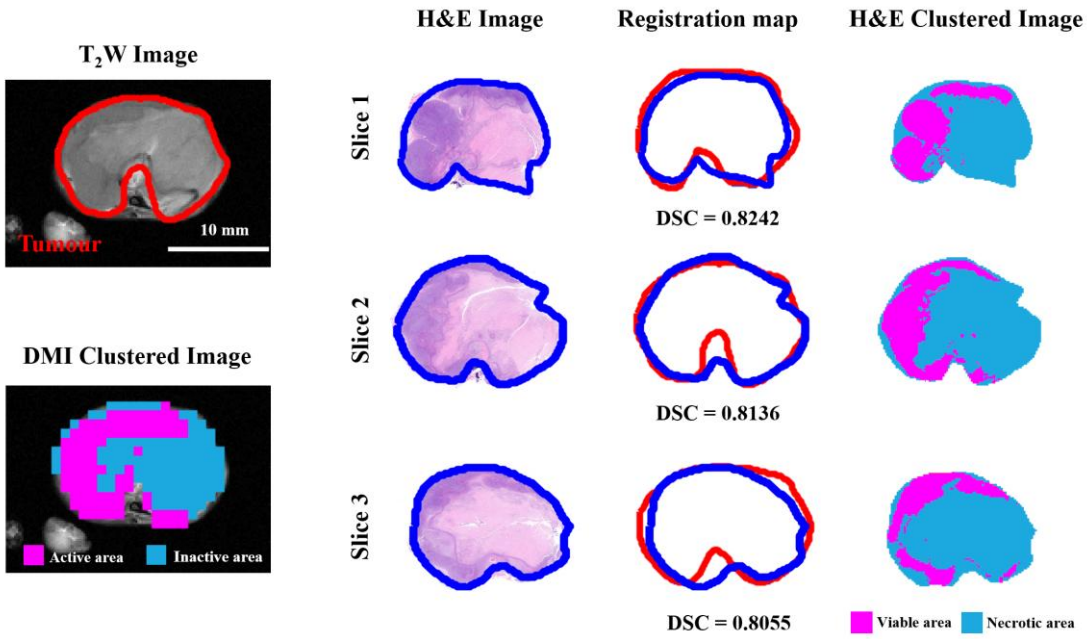

Figure S17. Assessment of through-plane histological consistency within the 6-mm DMI slice. Representative T_2-weighted MRI and the corresponding DMI-based clustered image are shown on the left. The red contour on the T_2-weighted image indicates the tumor boundary. In the DMI clustered image, magenta and cyan indicate metabolically active and inactive regions, respectively. To evaluate the potential effect of the 6-mm DMI slice thickness on MRI–histology comparison, serial H&E sections were obtained at approximately 2-mm intervals across the DMI slice volume. For each histological section, the original H&E image, MRI–histology registration map, and H&E-based viable/necrotic clustering result are shown. In the registration maps, red and blue contours indicate the tumor boundaries derived from MRI and histology, respectively, and the Dice similarity coefficient (DSC) quantifies boundary agreement after registration. The three serial sections showed broadly consistent large-scale viable and necrotic tissue patterns, supporting the use of central-plane histology for spatial correspondence analysis with DMI-defined metabolic compartments. Nevertheless, each histological section represents only a thin plane within the 6-mm DMI slice, and the MRI–histology comparison should therefore be interpreted as localized spatial validation rather than complete volumetric validation. In the H&E clustered images, magenta indicates viable tissue and cyan indicates necrotic tissue. These MRI and DMI clustering images are reused from Figs.1 and 3 to provide the anatomical and metabolic reference for comparison with serial histological sections.

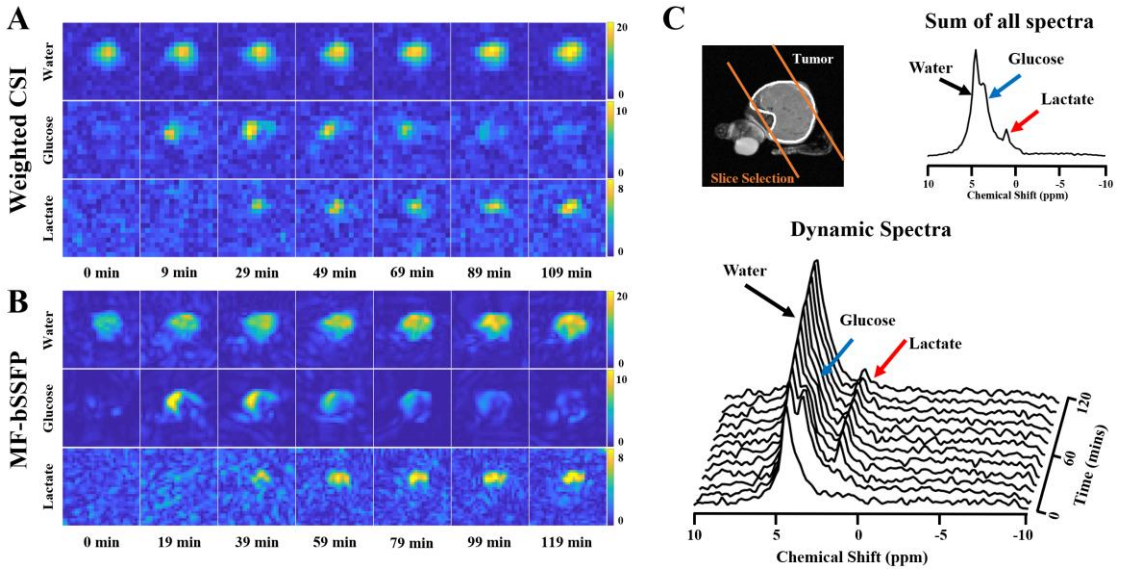

Figure S18. Dynamic ^{2}H metabolic imaging and slice-selected spectroscopy used to identify detectable resonances in a representative C26 tumor. (A) Dynamic DMI maps of water, glucose, and lactate obtained using weighted CSI in the same C26 tumor-bearing mouse. Weighted CSI was acquired with a 16 × 16 matrix, 1.8 × 1.8 mm^2 in-plane resolution. **(B)** Corresponding dynamic DMI maps obtained using MF-bSSFP. MF-bSSFP was acquired with a 32 × 32 matrix, 0.9 × 0.9 mm^2 in-plane resolution, providing improved spatial detail while showing temporal trends consistent with weighted CSI. **(C)** Slice-selected ^{2}H spectra acquired from the tumor region using NSPECT. The selected slice is indicated by the orange line on the axial ^{1}H T_2-weighted image. The summed and dynamic spectra demonstrate that water, glucose, and lactate were the dominant detectable resonances in this colorectal tumor model. No reliable Glx resonance was detected; therefore, Glx was not included as a separate component in the MF-bSSFP reconstruction

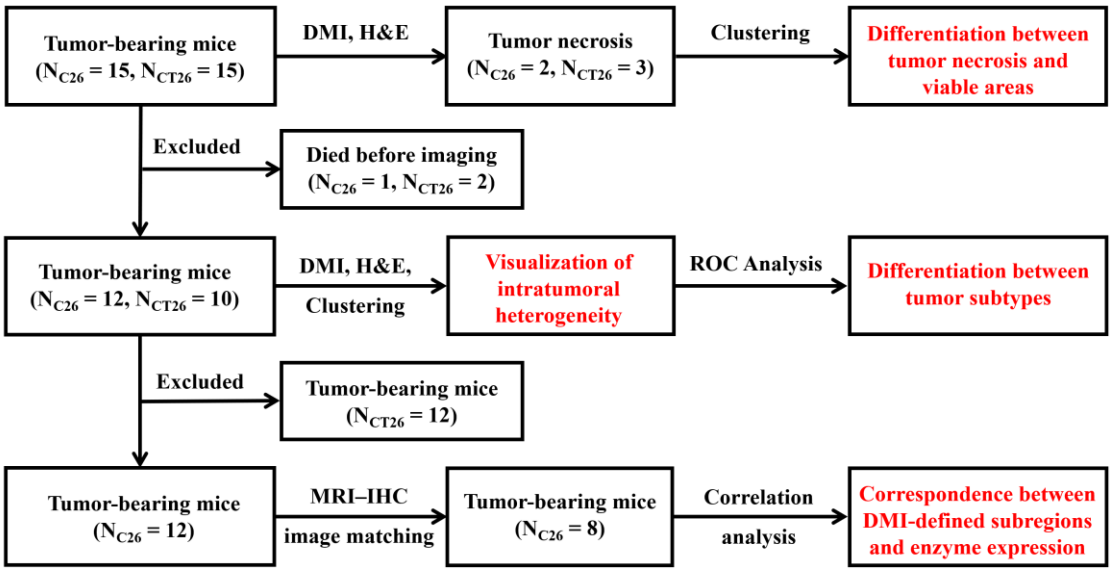

Figure S19. Summary of the in vivo experimental workflow adopted in this study. Thirty tumor-bearing mice were initially included, comprising fifteen C26 and fifteen CT26 tumor-bearing mice. During tumor growth before imaging, one C26 mouse and two CT26 mice died. All remaining mice underwent DMI scanning followed by H&E staining analysis. Two C26 and three CT26 tumors showed extensive necrosis; clustering analyses demonstrated that DMI could distinguish necrotic regions from viable tumor areas in these cases. The remaining twelve C26 and ten CT26 tumor-bearing mice, which did not show extensive necrosis, were used to assess intratumoral metabolic heterogeneity by clustering analysis and to differentiate between C26 and CT26 tumor models using ROC analysis. IHC analyses were performed in the twelve C26 tumor-bearing mice. Four mice were excluded from the IHC correlation analysis because their IHC sections could not be adequately spatially aligned with the corresponding MR images. Correlation analyses were therefore performed in the remaining eight C26 tumors with good MRI–histology spatial alignment, showing correspondence between DMI-defined metabolic subregions and the expression of metabolism-related markers.

Section 3 Tables

Table S1 Quantitative results of clustering evaluation indicators for C26 tumor-bearing mice

Mean Silhouette coefficient		Davies-Bouldin index		Calinski-Harabasz index	
K-means	PCA+GMM	K-means	PCA+GMM	K-means	PCA+GMM
0.6283	0.5285	0.7809	1.0444	178.7195	92.4296
0.5390	0.2988	0.8371	1.5244	87.6799	28.4093
0.6340	0.4099	0.7183	1.2248	187.2408	56.5430
0.6745	0.4692	0.6745	1.1657	143.5702	54.0468
0.6319	0.4565	0.7876	1.2415	354.5295	108.9568
0.6429	0.5157	0.7125	1.0105	230.1860	127.2432
0.6111	0.4856	0.7949	1.1579	208.8346	99.1640
0.6201	0.4097	0.7573	1.3670	152.2459	59.9307
0.5589	0.4604	0.9348	1.0868	150.1098	93.3838
0.6133	0.3600	0.7265	1.3966	131.5992	50.8816
0.6310	0.4563	0.7885	1.3163	204.8983	89.7979
0.6397	0.4430	0.7323	1.0748	302.7843	125.8242

Table S2 Quantitative results of clustering evaluation indicators for CT26 tumor-bearing mice

Mean Silhouette coefficient		Davies-Bouldin index		Calinski-Harabasz index	
K-means	PCA+GMM	K-means	PCA+GMM	K-means	PCA+GMM
0.6253	0.4209	0.7937	1.3665	281.1559	120.3940
0.6177	0.4741	0.7670	1.1146	163.0914	63.0230
0.6273	0.4894	0.6905	1.0097	168.5160	79.4959
0.5402	0.4908	0.9524	1.5929	232.4746	103.9922
0.6199	0.4726	0.7783	1.0384	129.0520	79.5921
0.7236	0.5864	0.6969	0.9483	321.5558	166.0909
0.5235	0.1474	0.8887	2.1586	116.8281	28.5438
0.5580	0.5195	0.8431	1.5222	150.3957	64.3526
0.5958	0.3916	0.8234	1.6876	412.7431	130.8099
0.6114	0.5777	0.8174	1.3467	370.0066	137.5904

Table S3 Metabolic pathways and main functions targeted by metabolism-related markers

metabolism-related markers	Metabolic pathway	Function in tumor metabolism
GLUT1	Glucose uptake	Mediates glucose transport across the plasma membrane and supports glycolytic metabolism
DLAT	Pyruvate oxidation	E2 component of the pyruvate dehydrogenase complex; catalyzes acetyl-group transfer to CoA, leading to acetyl-CoA formation
LDHA	Lactate production	Catalyzes the reduction of pyruvate to lactate and supports glycolytic metabolism.
MCT4	Lactate efflux	Exports lactate and H^+ from highly glycolytic cells and contributes to extracellular acidification
MCT1	Lactate transmembrane transport	Mediates lactate uptake or export depending on transmembrane lactate and proton gradients
HIF1α	Hypoxia-responsive transcriptional regulation	Activates hypoxia- and glycolysis-related genes and promotes metabolic adaptation to low oxygen
PKM2	Downstream glycolysis	Regulates glycolytic flux and can influence gene programs associated with proliferation
AKT	Glucose uptake and anabolic metabolism	Promotes glucose uptake, glycolysis, and lipid synthesis

Table S4 Two-way ANOVA summary of metabolism-related markers expression across DMI-based phenotypes

Marker	Glucose main effect (HG vs LG)	Lactate main effect (HL vs LL)	Interaction (G×L)	Interpretation
GLUT1	P<0.0001 (HG>LG)	p=0.5955 (n.s.)	p=0.9682 (n.s.)	aligns with Glucose axis (higher in HG)
DLAT	P<0.0001 (HG>LG)	p=0.2455 (n.s.)	p=0.0130	Primarily aligns with Glucose axis (HG > LG), with significant G×L modulation
MCT4	p=0.5141 (n.s.)	P<0.0001 (HL>LL)	p=0.3638 (n.s.)	Aligns with Lactate axis (higher in HL)
LDHA	p=0.6382 (n.s.)	P<0.0001 (HL>LL)	p=0.1823 (n.s.)	Aligns with Lactate axis (higher in HL)